

Interlayer exchange coupling effects on the spin-orbit torque in synthetic magnets

Haodong Fan(樊浩东), Zhongshu Feng(冯重舒), Tingwei Chen(陈亭伟), Xiaofeng Han(韩晓峰), Xinyu Shu(舒新愉), Mingzhang Wei(卫鸣璋), Shiqi Liu(刘士琦), Mengxi Wang(王梦溪), Shengru Chen(陈盛如), Xuejian Tang(唐学健), Menghao Jin(金蒙豪), Yungui Ma(马云贵), Bo Liu(刘波), and Tiejun Zhou(周铁军)
Citatio: Chin. Phys. B, 2025, 34 (**9**): 098501. DOI: 10.1088/1674-1056/ade42c
http://cpb.iphy.ac.cn; http://iopscience.iop.org/cpb

What follows is a list of articles you may be interested in

Spatial electron-spin splitting in single-layered semiconductor microstructure modulated by Dresselhaus spin-orbit coupling

Jia-Li Chen(陈嘉丽), Sai-Yan Chen(陈赛艳), Li Wen(温丽), Xue-Li Cao(曹雪丽), and Mao-Wang Lu(卢卯旺)
Chin. Phys. B, 2024, 33 (**11**): 118501. DOI: 10.1088/1674-1056/ad6b83

Influence of exchange bias on spin torque ferromagnetic resonance for quantification of spin-orbit torque efficiency

Qian Zhao(赵乾), Tengfei Zhang(张腾飞), Bin He(何斌), Zimu Li(李子木), Senfu Zhang(张森富), Guoqiang Yu(于国强), Jianbo Wang(王建波), Qingfang Liu(刘青芳), and Jinwu Wei(魏晋武)
Chin. Phys. B, 2024, 33 (**5**): 058502. DOI: 10.1088/1674-1056/ad2d55

Interfacial DMI in Fe/Pt thin films grown on different buffer layers

Wen-Jun Zhang(张文君), Fei Wei(魏菲), Bing Liu(刘冰), Yang Zhou(周阳), Shi-Shou Kang(康仕寿), and Bing Sun(孙兵)
Chin. Phys. B, 2024, 33 (**4**): 048501. DOI: 10.1088/1674-1056/ad1b41

Valleytronic topological filters in silicene-like inner-edge systems

Hang Xie(谢航), Xiao-Long Lü(吕小龙), and Jia-En Yang(杨加恩)
Chin. Phys. B, 2024, 33 (**1**): 018502. DOI: 10.1088/1674-1056/ad0714

Perpendicular magnetization switching by large spin—orbit torques from sputtered Bi_2Te_3

Zhenyi Zheng(郑臻益), Yue Zhang(张悦), Daoqian Zhu(朱道乾), Kun Zhang(张昆), Xueqiang Feng(冯学强), Yu He(何宇), Lei Chen(陈磊), Zhizhong Zhang(张志仲), Dijun Liu(刘迪军), Youguang Zhang(张有光), Pedram Khalili Amiri, Weisheng Zhao(赵巍胜)
Chin. Phys. B, 2020, 29 (**7**): 078505. DOI: 10.1088/1674-1056/ab9439

RAPID COMMUNICATION

Interlayer exchange coupling effects on the spin–orbit torque in synthetic magnets

Haodong Fan(樊浩东)[1,2], Zhongshu Feng(冯重舒)[3], Tingwei Chen(陈亭伟)[2], Xiaofeng Han(韩晓峰)[3], Xinyu Shu(舒新愉)[3], Mingzhang Wei(卫鸣璋)[3], Shiqi Liu(刘士琦)[2], Mengxi Wang(王梦溪)[2], Shengru Chen(陈盛如)[2], Xuejian Tang(唐学健)[2], Menghao Jin(金蒙豪)[3], Yungui Ma(马云贵)[1], Bo Liu(刘波)[2,†], and Tiejun Zhou(周铁军)[2,3,‡]

[1] *State Key Laboratory of Modern Optical Instrumentation, Centre for Optical and Electromagnetic Research, College of Optical Science and Engineering, Zhejiang University, Hangzhou* 310058, *China*

[2] *State Key Laboratory of Spintronic Devices and Technologies, Hangzhou* 311305, *China*

[3] *School of Electronics and Information, Hangzhou Dianzi University, Hangzhou* 310018, *China*

(Received 12 May 2025; revised manuscript received 12 June 2025; accepted manuscript online 13 June 2025)

Interlayer exchange coupling (IEC) plays a critical role in spin–orbit torque (SOT) switching in synthetic magnets. This work establishes a fundamental correlation between IEC and SOT dynamics within Co/Pt-based synthetic antiferromagnets and synthetic ferromagnets. The antiferromagnetic and ferromagnetic coupling states are precisely engineered through Ruderman–Kittel–Kasuya–Yosida (RKKY) interactions by modulating the Ir spacer thickness. Experimental results reveal that the critical switching current density exhibits a strong positive correlation with the IEC strength, regardless of the coupling type. A comprehensive theoretical framework based on the Landau–Lifshitz–Gilbert equation elucidates how IEC contributes to the effective energy barrier that must be overcome during SOT-induced magnetization switching. Significantly, the antiferromagnetically coupled samples demonstrate enhanced SOT efficiency, with the spin Hall angle being directly proportional to the antiferromagnetic exchange coupling field. These insights establish a coherent physical paradigm for understanding IEC-dependent SOT dynamics and provide strategic design principles for the development of energy-efficient next-generation spintronic devices.

Keywords: interlayer exchange coupling, spin–orbit torque, synthetic antiferromagnet

PACS: 85.75.–d, 75.60.Jk, 85.70.Ay

DOI: 10.1088/1674-1056/ade42c **CSTR:** 32038.14.CPB.ade42c

1. Introduction

Spin-orbit torque (SOT), fundamentally driven by the spin Hall effect[1,2] or Rashba–Edelstein effect,[3] represents a key writing mechanism for next-generation magnetic random access memory. SOT offers substantial performance advantages, including reduced energy consumption, increased operational speed, and highly reliable non-volatility,[4–9] along with remarkable efficiency in magnetic switching,[10–12] magnetization dynamics control,[13] and magnetic domain propagation.[14] Conventional SOT architectures predominantly utilize heavy metal/ferromagnet (HM/FM) bilayers. However, as ferromagnetic spintronic devices undergo progressive miniaturization, static magnetic crosstalk between adjacent memory cells inevitably constrains storage density. In response to these constraints, recent advances in spin-split antiferromagnet-based all-electric read/write mechanisms have attracted significant attention,[15] since antiferromagnets (AFMs) exhibit zero net magnetic moment and superior resistance to magnetic interference. Nevertheless, spin-split antiferromagnets, including non-collinear antiferromagnets[16–18] and altermagnets,[19] typically require quasi-epitaxial growth on single-crystal substrates,[20] presenting substantial compatibility challenges with current industrial manufacturing protocols.[21]

Perpendicularly magnetized synthetic antiferromagnets (SAFs) are promising storage media for state-of-the-art magnetic memories and logic devices, effectively integrating the advantages of FM and AFM.[22–25] SAFs exhibit exceptional properties, including enhanced thermal stability, compensated magnetization, reduced stray fields, and tunable interlayer exchange coupling[26] (IEC) through Ruderman–Kittel–Kasuya–Yosida (RKKY) interactions.[27–32] The IEC significantly influences the SOT characteristics of SAFs, with SOT-induced switching confined between two antiparallel states.[13,33] Notably, SAFs typically demonstrate superior SOT efficiency compared to synthetic ferromagnets (SFs).[34,35] However, the detailed mechanism through which IEC modulates the SOT switching current density remains elusive, hindering the further development of energy-efficient SAF-based spintronic devices. A systematic investigation of IEC-tuned SOT effects across both SAF and SF systems is

†Corresponding author. E-mail: liubo@spinlab.cn

‡Corresponding author. E-mail: tjzhou@hdu.edu.cn

© 2025 Chinese Physical Society and IOP Publishing Ltd. All rights, including for text and data mining, AI training, and similar technologies, are reserved.

therefore essential for understanding the underlying physics and optimizing device performance.

Here, we systematically investigate the effects of IEC on magnetization switching, switching current density, and SOT efficiency in SAF and SF structures. A typical antiferromagnetic coupling system with IEC featuring RKKY oscillatory decay characteristics is first constructed. The results show oscillations in both the critical switching current (I_c) and the switching current density (J_c) with varying Ir thickness, which can be attributed to fluctuations in the IEC strength. It is noteworthy that J_c is positively correlated with IEC strength, irrespective of the coupling nature (antiferromagnetic or ferromagnetic). Further analysis based on the Landau–Lifshitz–Gilbert equation reveals that the total effective energy barrier to be overcome during SOT switching increases with IEC strength. Additionally, a positive correlation is demonstrated between the effective spin Hall angle and the antiferromagnetic exchange coupling field. These correlations offer a strategic approach for enhancing SOT efficiency and reducing J_c in SAF and SF structures, thereby paving the way for the development of SAF-based devices for low-power and high-speed non-volatile memory applications.

2. Experiments

All films were fabricated on thermally oxidized Si/SiO_2 substrates using a magnetron sputtering system (AJA Int., Inc.) with a base vacuum pressure below 4×10^{-5} mTorr at ambient temperature. As illustrated in Fig. 1(a), a Pt layer of 5 nm thickness serves as the spin source, while the stack structures of FM1 and FM2 consist of Co(0.53)/Pt(0.3)/Co(0.53) and Co(0.3)/Pt(0.3)/Co(0.3) (in units of nanometer), respectively. The sputtering rate for each layer was pre-calibrated through x-ray reflection measurements. The Co thickness was chosen to ensure perpendicular magnetic anisotropy (PMA) in both FM1 and FM2, with the intermediate Pt (0.3 nm) layer incorporated to enhance PMA. The Ir thickness (t_{Ir}) was varied between 0.5 nm and 1.7 nm to modulate the IEC, since an Ir layer below this range would become discontinuous, whereas a thicker Ir layer would result in a diminished IEC. Furthermore, a 1 nm Ta layer was deposited between the bottom Pt layer and the substrate to enhance film adhesion, while a protective 1.5 nm Ta capping layer was grown on the film surface to prevent oxidation.

For magnetotransport measurements, Hall bar devices with dimensions of 34 μm in length and 5 μm in width were fabricated through a standard photolithography process followed by argon ion etching. The deposition of Cr/Au electrodes was subsequently accomplished via a secondary lithography and lift-off process. The optical microscope image of the fabricated Hall bar and the measurement setup are illustrated in Fig. 1(b), with the effective film located at the central cross region of the electrode. Magnetotransport characterization was carried out in a superconducting magnet system using a standard four-terminal method. All measurements were performed at room temperature. The anomalous Hall voltages were detected by applying current along the x-direction, subjecting the sample to a varying magnetic field in the z-direction, and measuring the resultant signal in the y-direction with a lock-in amplifier. In current-induced SOT switching measurements, a pulse current with a duration of 30 μs was applied, and the Hall resistance was subsequently recorded using a small alternating excitation current. A polar magneto-optical Kerr microscope (PMOKE) was used to visualize the magnetization switching process for SAF. For the characterization of SOT efficiency in SAF and SF, an external magnetic field was rotated within the xz plane, clockwise and counterclockwise in each revolution.

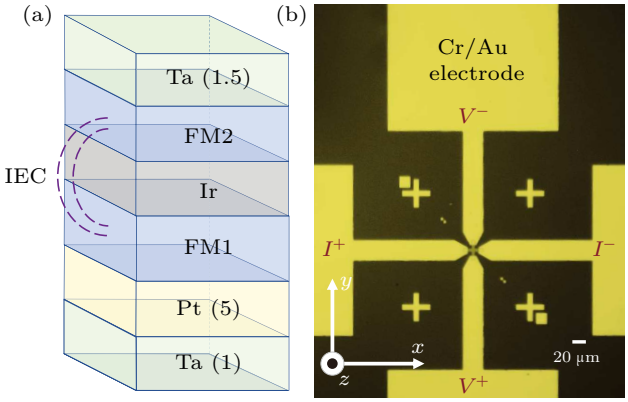


Fig. 1. (a) Structural schematic of SAF. (b) A representative microscopic image of the Hall bar, along with the corresponding measurement scheme.

3. Results

3.1. Determination of IEC

The magnetic properties of the films were characterized using vibrating sample magnetometer (VSM) measurements, with a representative sample ($t_{Ir} = 1.5$ nm) shown in Fig. 2. The presence of multiple switching steps confirms robust antiferromagnetic IEC, while the pronounced rectangular hysteresis loops verify strong PMA in both FM layers. A saturation magnetization of approximately 1250 emu/cm^3 indicates negligible interfacial dead layer formation.

The antiferromagnetic exchange coupling field (H_{ex}) was extracted by evaluating the horizontal displacement of minor hysteresis loops as the external magnetic field was gradually reduced. The H_{ex} values derived from VSM measurements show excellent agreement with those obtained from anomalous Hall effect (AHE) characterization. However, a noticeable discrepancy exists between the VSM and AHE curves due to different measurement configurations: AHE was performed on patterned Hall bar devices, whereas the M–H_z curve was obtained from the continuous film. Specifically, the 5 μm

wide Hall bar exhibits a slightly enhanced switching field relative to the unpatterned film, attributed to pinning effects introduced during microfabrication. Thermal effects are negligible owing to the weak alternating current used in AHE. Additionally, the amplitude differences observed in intermediate minor loops originate primarily from current shunting effects inherent to transverse resistivity measurements in AHE.

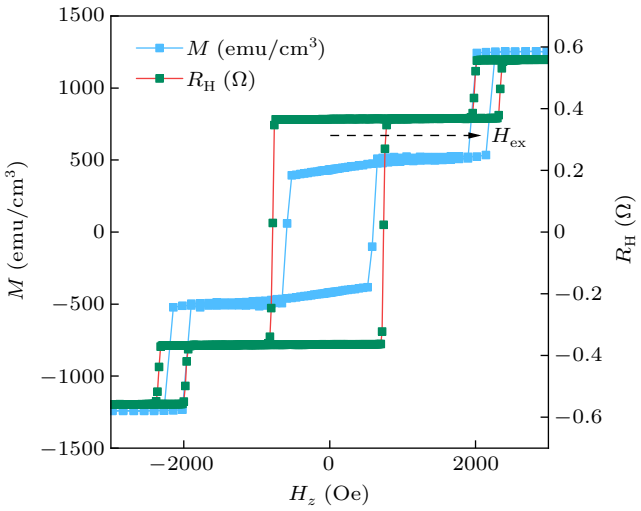


Fig. 2. VSM and AHE measurements obtained at t_{Ir}=1.5 nm. The definition of the H_{ex} is also sketched.

A comprehensive AHE study was carried out on all devices to investigate magnetization switching dynamics. The samples were classified into three regimes according to the Ir interlayer thickness (t_{Ir})

- Strong antiferromagnetic coupling ($t_{Ir} = 0.5$–0.7 nm)
- Ferromagnetic coupling ($t_{Ir} = 0.8$–1.3 nm)
- Weak antiferromagnetic coupling ($t_{Ir} = 1.4$–1.7 nm)

As shown in Figs. 3(a)–3(c), all devices exhibit robust PMA. When t_{Ir} increases from 0.5 to 0.7 nm, H_{ex} decreases from 4 T to 1.7 T, reflecting strong antiferromagnetic coupling tuned by the Ir spacer.[36] For the representative case of $t_{Ir} = 0.7$ nm, magnetic moments in both FM layers align with the external field (H_z) once H_z exceeds H_{ex}.[37,38] Given the thickness-dependent scaling of anomalous Hall resistance (R_H) with magnetization, and the fact that FM2 is thinner than FM1, preferential switching of FM2 occurs during gradual field reduction.[34] Below H_{ex}, the dominant antiferromagnetic coupling enforces antiparallel alignment of FM1 and FM2, leading to sequential transitions during field polarity reversal

$$\downarrow\downarrow \rightarrow \uparrow\downarrow \rightarrow \downarrow\uparrow \rightarrow \uparrow\uparrow,$$

as illustrated in Fig. 3(a).

In the intermediate range ($t_{Ir} = 0.8$–1.3 nm), synchronous switching of FM1 and FM2 is observed, characteristic of ferromagnetic interlayer coupling,[39] with only two stable states: '$\downarrow\downarrow$' and '$\uparrow\uparrow$'. At larger thicknesses ($t_{Ir} = 1.4$–1.7 nm), a secondary antiferromagnetic coupling regime emerges, with a reduced H_{ex} (0.21 T at $t_{Ir} = 1.5$ nm). Notably, the maximum H_{ex} values of 4 T and 0.21 T are recorded at $t_{Ir} = 0.5$ nm and $t_{Ir} = 1.5$ nm, respectively, consistent with previous studies.[36,40]

The dependence of R_H and H_{ex} on t_{Ir} is summarized in Figs. 3(d) and 3(e). R_H decreases linearly with increasing t_{Ir}, consistent with earlier reports.[34] This behavior is explained by the parallel shunt model: as the Ir layer thickens, more current bypasses the FM layers, reducing the Hall voltage contribution. The thickness dependence of H_{ex} was fitted using the RKKY form

$$H_{ex} \propto \frac{\sin(\phi + 2\pi t_{Ir}/\lambda_F)}{t_{Ir}^2}, \tag{1}$$

where $\phi = -5.12$ and $\lambda_F = 1$ nm are the phase and Fermi wavelength of Ir, respectively. The fitting incorporates the antiferromagnetic coupling regions ($t_{Ir} = 0.5$–0.7 nm and $t_{Ir} = 1.4$–1.7 nm). Although AHE loops yield $H_{ex} = 0$ in the ferromagnetic region, this does not imply absence of IEC; instead, the coupling strength can be inferred from the fitted curve, with opposite sign relative to antiferromagnetic coupling.

These results establish the fundamental framework for understanding how IEC modulates SOT switching behavior in SAF and SF systems.

3.2. IEC dependent switching current density

The influence of IEC on SOT-induced magnetization switching is systematically investigated in this subsection. Current-induced magnetization switching measurements of two representative samples — an SAF with $t_{Ir} = 0.5$ nm and an SF with $t_{Ir} = 1.1$ nm — under various in-plane auxiliary magnetic fields (H_x) are shown in Figs. 4(a) and 4(b), respectively. The opposite switching polarities observed under different H_x polarities arise from the spin Hall effect in the bottom Pt layer, which generates an upward spin current. As a result, counterclockwise switching polarity is observed for positive H_x and clockwise polarity for negative H_x.

The bottom FM switches first because it is directly in contact with the spin source. A slight reduction in ΔR_H is observed at $H_x = \pm 100$ Oe, and switching is suppressed in the absence of an auxiliary field due to insufficient symmetry breaking. Remarkably, robust switching persists even at $H_x = \pm 3000$ Oe, underscoring the excellent anti-interference capability of both SAF and SF structures.[42] Correlating the AHE results with the switching resistance ΔR_H confirms that magnetization switching in the SAF occurs between two antiparallel states, characteristic of typical SOT switching in SAF (Fig. 4(a)).[35,37,43] Although the ΔR_H for current-driven switching is slightly smaller than for field-driven switching, it still represents full magnetization reversal. This difference arises because field-driven switching affects the entire Hall

bar area, whereas current-driven switching only reverses magnetization within the current channel, leaving voltage measurement regions unswitched — a result further confirmed by PMOKE.

The SAF switching was directly visualized using PMOKE. Under a −22 mA current pulse, black and white regions represent downward and upward magnetized states of the bottom FM layer at $H_x = +1200$ and −1200 Oe, respectively. As shown in Fig. 5, switching first occurs at the edges of the current path and then gradually expands to the Hall bar crossing. By contrast, the SF exhibits switching between two parallel states, indicative of synchronous switching of the two FM layers (Fig. 4(b)).

The critical switching current (I_c) is defined as the current corresponding to 50% of the total ΔR_H switching. All samples exhibit full magnetization switching with the aid of an in-plane magnetic field, allowing precise extraction of I_c. The oscillatory dependence of I_c on t_{Ir} at $H_x = 500$ Oe is summarized in Fig. 4(c). Specifically, lower I_c values appear at transition points between AFM and FM coupling ($t_{Ir} = 0.8$ nm or 1.3–1.4 nm), whereas higher I_c values occur under strong AFM coupling ($t_{Ir} = 0.5$ or 1.5 nm) and strong FM coupling ($t_{Ir} = 1.0$ nm).

Accounting for the current shunt effect and incorporating the resistivity and thickness of each metallic layer,[44] the critical switching current density J_c (switching current per unit area) is obtained as a function of t_{Ir} (Fig. 4(d)). J_c exhibits an oscillatory pattern similar to that of I_c, and its dependence on t_{Ir} closely follows the IEC strength derived from RKKY fitting.[45] The measured J_c ranges from $(4.1–5.3) \times 10^7$ A/cm^2, consistent with values reported for SAF.[35,46] As shown in Fig. 4(e), H_{ex} for AFM coupling is experimentally measured, while H_{ex} for FM coupling is inferred from RKKY fitting. Strikingly, J_c is positively correlated with the IEC strength, regardless of whether the coupling is AFM or FM, as confirmed by the dashed linear fit.

It is worth noting that thickness variation of the Ir layer has a negligible effect on J_c for two reasons. First, the spin Hall angle of Ir (~ 0.02)[47] is significantly smaller than that of Pt, yielding only a minor spin current contribution. Second, Ir and Pt have the same spin Hall angle sign, which could in principle lead to partial cancellation if both injected spin currents reach the bottom Co layer. However, no corresponding increase in J_c was experimentally observed.

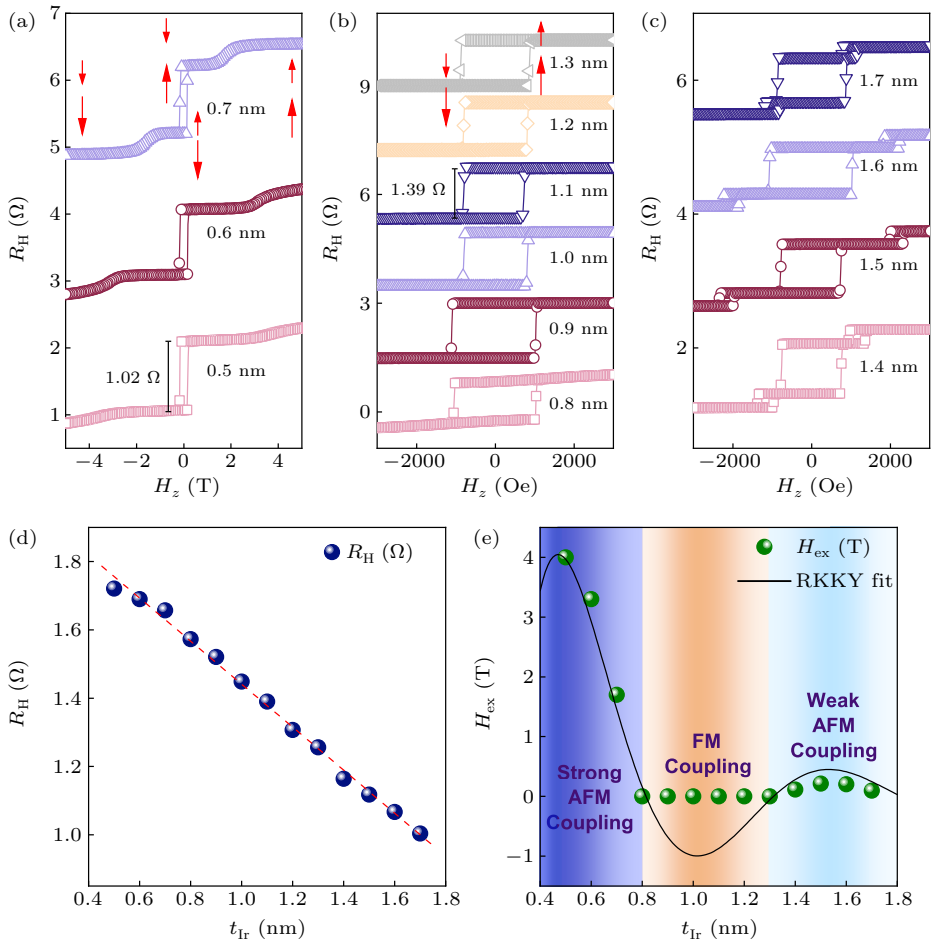


Fig. 3. (a)–(c) AHE measurements for samples with varying Ir thicknesses. The red arrows indicate the magnetic moment orientation in the upper and lower FM layers. (d) Anomalous Hall resistance (R_H) as a function of Ir thickness, with the dashed line indicating a linear fit of R_H versus t_{Ir}. (e) H_{ex} plotted against t_{Ir}, demonstrating characteristic RKKY oscillatory decay behavior. Different background colors denote distinct coupling regimes.

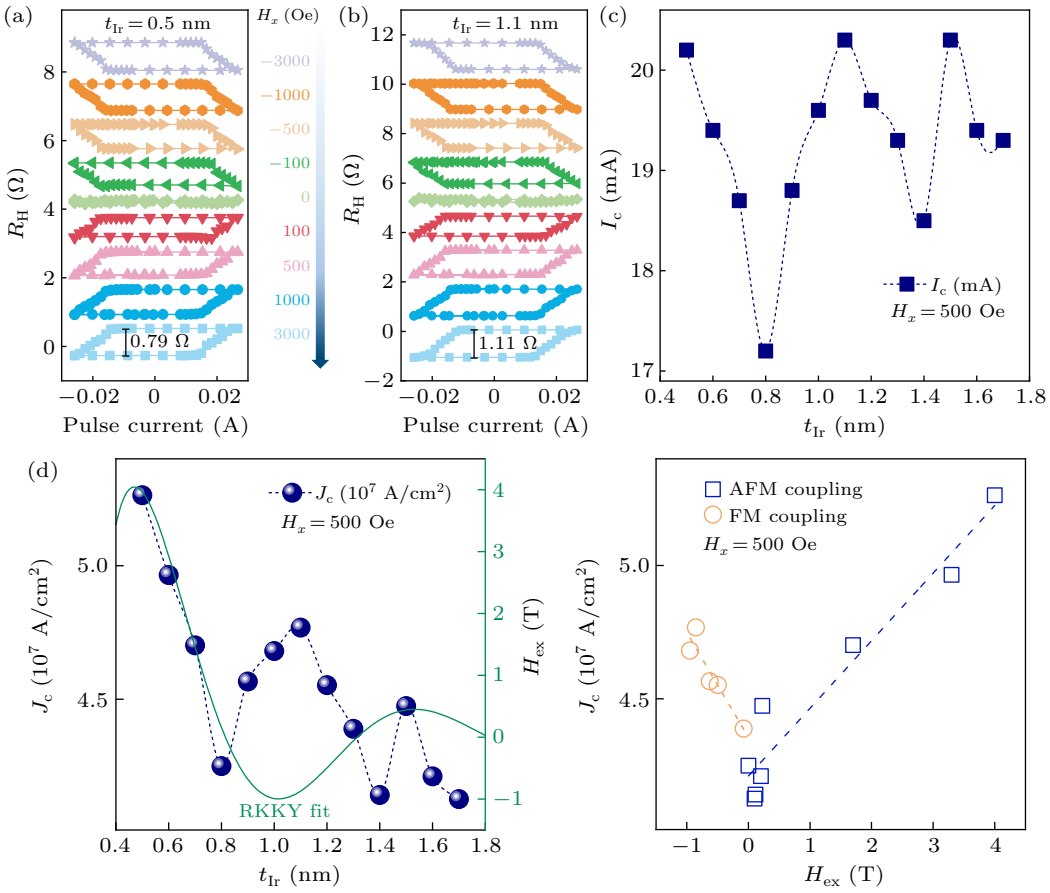


Fig. 4. Current-induced magnetization switching at (a) $t_{Ir} = 0.5$ nm and (b) $t_{Ir} = 1.1$ nm under different in-plane magnetic fields. The arrows and numbers denote the sequence of applied H_x. (c) I_c and (d) J_c as functions of t_{Ir} at $H_x = 500$ Oe. The solid curve shows the RKKY fitting. (e) Correlation between J_c and H_{ex} at $H_x = 500$ Oe. AFM and FM couplings are represented by navy squares and orange circles, respectively. The dashed lines indicate linear fits.

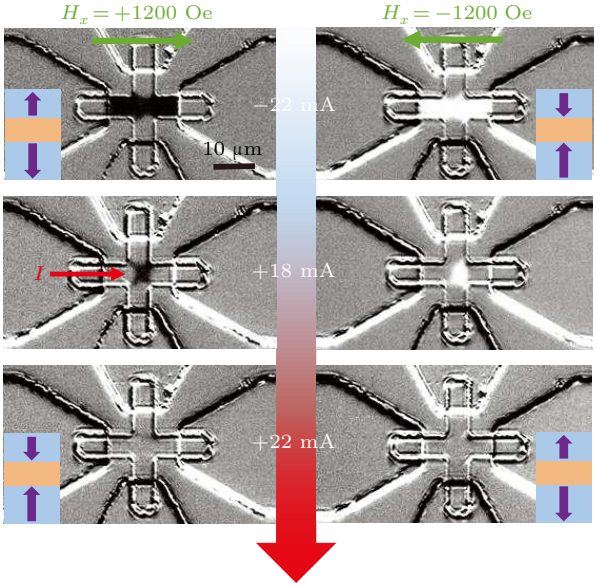


Fig. 5. The domain-wall evolution observed using PMOKE for a $t_{Ir} = 1.5$ nm sample under $H_x = \pm 1200$ Oe. The pulse current width is 120 μs. The inset shows the magnetic moment orientation of the synthetic antiferromagnet before and after SOT switching.

3.3. Theoretical explanation based on LLG equation

To elucidate the positive correlation between J_c and H_{ex}, a plausible explanation based on the Landau–Lifshitz–Gilbert (LLG) equation is proposed. The magnetization dynamics of the HM/FM structure can be described by the LLG equation[48]

$$\frac{\mathrm{d}\boldsymbol{m}}{\mathrm{d}t} = -\gamma \boldsymbol{m} \times \boldsymbol{H}_{\mathrm{EFF}} + \alpha \boldsymbol{m} \times \frac{\mathrm{d}\boldsymbol{m}}{\mathrm{d}t} - \gamma H_{\mathrm{DL}} \boldsymbol{m} \times (\boldsymbol{m} \times \boldsymbol{\sigma}), \tag{2}$$

where $\boldsymbol{m}$ represents the magnetization unit vector, α denotes the Gilbert damping constant, γ corresponds to the gyromagnetic ratio, and $\boldsymbol{\sigma}$ signifies the spin polarization vector, which is assumed to be collinear with the y-axis. H_{DL} is the damping-like effective field responsible for driving SOT magnetization switching. The effective magnetic field acting on $\boldsymbol{m}$, denoted as $\boldsymbol{H}_{\mathrm{EFF}}$, encompasses the external magnetic field ($\boldsymbol{H}_{\mathrm{ext}}$), the anisotropy field ($\boldsymbol{H}_{\mathrm{k}}$), and the interlayer exchange coupling field ($\boldsymbol{H}_{\mathrm{IEC}}$).

Next, we consider two magnetic layers (denoted as 1 and 2), which may be coupled either antiferromagnetically or ferromagnetically. Assuming the SOT only acts on FM1, the LLG equations for the unit magnetization vectors $\boldsymbol{m}_{1(2)}$ of layers 1 and 2 are

$$\frac{\mathrm{d}\boldsymbol{m}_1}{\mathrm{d}t} = -\gamma \boldsymbol{m}_1 \times (\boldsymbol{H}_{\mathrm{ext}} + \boldsymbol{H}_{k1} + \boldsymbol{H}_{\mathrm{IEC1}})$$

$$+\alpha \boldsymbol{m}_1 \times \frac{\mathrm{d}\boldsymbol{m}_1}{\mathrm{d}t} - \gamma H_{\mathrm{DL}} \boldsymbol{m}_1 \times (\boldsymbol{m}_1 \times \boldsymbol{\sigma}), \quad (3)$$

$$\frac{\mathrm{d}\boldsymbol{m}_2}{\mathrm{d}t} = -\gamma \boldsymbol{m}_2 \times (\boldsymbol{H}_{\mathrm{ext}} + \boldsymbol{H}_{k2} + \boldsymbol{H}_{\mathrm{IEC2}}) + \alpha \boldsymbol{m}_2 \times \frac{\mathrm{d}\boldsymbol{m}_2}{\mathrm{d}t}, \quad (4)$$

where $\boldsymbol{H}_{\mathrm{IEC1}} = J\boldsymbol{m}_2$, $\boldsymbol{H}_{\mathrm{IEC2}} = J\boldsymbol{m}_1$, and J is the exchange coupling constant. Considering that the IEC energy can be expressed as $\boldsymbol{E}_{\mathrm{IEC}} = -J\boldsymbol{m}_1 \cdot \boldsymbol{m}_2$, differentiating this energy with respect to the magnetic moment yields the IEC field acting on $\boldsymbol{m}_1$ as $\boldsymbol{H}_{\mathrm{IEC1}} = -\partial \boldsymbol{E}_{\mathrm{IEC}}/\partial \boldsymbol{m}_1 = J\boldsymbol{m}_2$. Since FM1 is positioned adjacent to the Pt (5) layer in the experimental design, the spin current generated within Pt (5) exerts torque exclusively on FM1; thus, Eq. (4) does not include the SOT term.

For antiferromagnetic coupling ($J < 0$), $\boldsymbol{H}_{\mathrm{IEC1}}$ is oriented opposite to $\boldsymbol{m}_2$, thereby inducing an antiparallel alignment between the two magnetization layers, whereas for ferromagnetic coupling ($J > 0$), $\boldsymbol{H}_{\mathrm{IEC1}}$ is oriented in the same direction as $\boldsymbol{m}_2$. Consequently, regardless of the coupling type, the magnitude of $\boldsymbol{H}_{\mathrm{IEC1}}$ increases with stronger IEC, resulting in a corresponding increase in the total effective field $\boldsymbol{H}_{\mathrm{EFF}}$, which resists the moment switching of FM1. According to established SOT theory, the damping-like effective field H_{DL} is proportional to the injected current density J_{c}, expressed as $H_{\mathrm{DL}} \propto J_{\mathrm{c}}$. Therefore, overcoming the total effective field $\boldsymbol{H}_{\mathrm{EFF}}$ necessitates an increase in H_{DL}, which directly results in an elevation of the critical switching current J_{c}.

3.4. IEC dependent SOT efficiency

The IEC can exert a significant influence on the SOT efficiency in SAF and SF systems. To elucidate this phenomenon, a fixed rotating external magnetic field is applied in the xz plane, where β denotes the angle of the rotating magnetic field relative to the x-axis.[35,43] For a sample with $t_{\mathrm{Ir}} = 0.5$ nm, the R_H–β curves exhibit opposite horizontal displacements when $I_{\mathrm{dc}} = \pm 12$ mA and $H_x = 3000$ Oe (Fig. 6(a)). This magnetization switching behavior can be attributed to the combined effects of the perpendicular component of the applied field and the spin–orbit torque. When $I_{\mathrm{dc}} = +12$ mA is applied, a spin current from the Pt layer is injected into the Co(0.53)/Pt(0.3)/Co(0.53) structure, generating an effective field in the $+z$ direction and contributing to H_z, which consequently results in a leftward shift. Conversely, applying $I_{\mathrm{dc}} = -12$ mA induces a rightward shift. The angular shift ($\Delta\beta$) for the SAF device with $t_{\mathrm{Ir}} = 0.5$ nm is measured to be 7.0° (Fig. 6(a)), whereas for the SF device with $t_{\mathrm{Ir}} = 1.0$ nm, $\Delta\beta$ is 1.55° (Fig. 6(b)). As demonstrated in Fig. 6(c), a linear relationship is observed between $\Delta\beta$ and I_{dc}, with the offset sign being directly correlated with the sign of H_x, which is recognized as a characteristic signature of SOT-induced effective fields.[49,50]

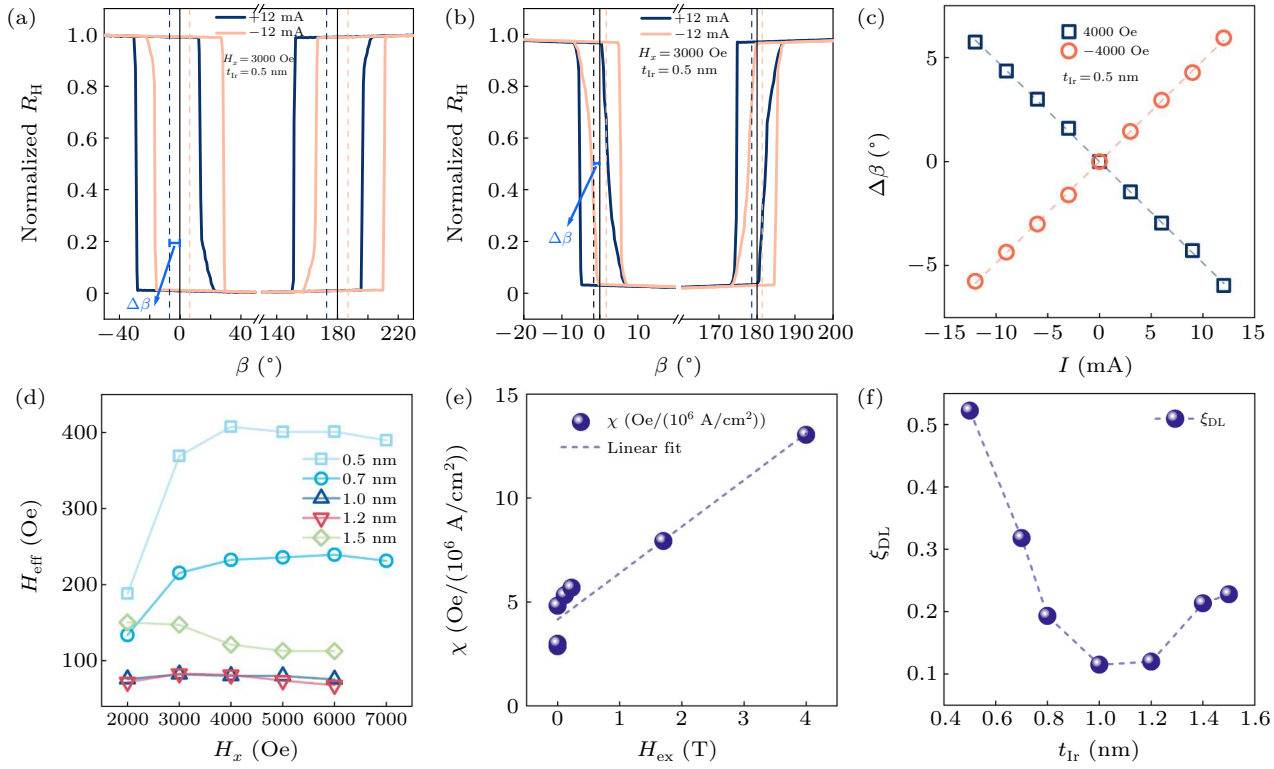


Fig. 6. Anomalous Hall curves for (a) $t_{\mathrm{Ir}} = 0.5$ nm, (b) $t_{\mathrm{Ir}} = 1.0$ nm obtained by rotating a 3000 Oe field in the xz plane while applying $I_{\mathrm{dc}} = \pm 12$ mA. (c) Angular displacement $\Delta\beta$ versus the dc current under $H_x = \pm 4000$ Oe with $t_{\mathrm{Ir}} = 0.5$ nm. (d) The SOT effective field H_{eff} versus H_x for representative t_{Ir}. (e) Saturation SOT efficiency χ versus H_{ex}. (f) Effective spin Hall angle, ξ_{DL}, as a function of t_{Ir}.

For small angles β, the z-component of the magnetic field can be approximated as $H_z = H_x \sin\beta \approx \beta H_x$. The SOT effective field H_{eff} is thus determined through the relation $H_{\text{eff}} = H_x\beta$. A summary of H_{eff} for representative Ir thickness samples under various external fields H_x is presented in Fig. 6(d). A striking feature is that H_{eff} is observed to initially increase to a maximum value before gradually decreasing with increasing H_x. Moreover, the magnitude of H_{eff} follows an approximate hierarchical trend: strong antiferromagnetic coupling > weak antiferromagnetic coupling > ferromagnetic coupling. The SOT efficiency χ, defined as the SOT effective field per unit current density, is calculated using $\chi = H_{\text{eff(sat)}}/J$, where $H_{\text{eff(sat)}}$ denotes the saturated SOT effective field. The saturation SOT efficiencies are determined to be 13.036 Oe/(10^6 A/cm^2), 7.937 Oe/(10^6 A/cm^2), 4.823 Oe/(10^6 A/cm^2), 2.870 Oe/(10^6 A/cm^2), 2.993 Oe/(10^6 A/cm^2), 5.324 Oe/(10^6 A/cm^2), and 5.687 Oe/(10^6 A/cm^2) for t_{Ir} values of 0.5 nm, 0.7 nm, 0.8 nm, 1.0 nm, 1.2 nm, 1.4 nm, and 1.5 nm, respectively. Interestingly, the SOT efficiency χ is proportional to H_{ex}, as shown in Fig. 6(e). This phenomenon is mainly caused by the magnetic domain wall propagation dynamics, where strong antiferromagnetic coupling ensures that the domain walls are tightly coupled during propagation.[35] In contrast, weak antiferromagnetic coupling may allow domain wall separation during propagation, preventing simultaneous switching of the upper and lower ferromagnetic layers. Considering the small variation in switching current density, the SOT efficiency decreases under weak coupling conditions relative to strong coupling scenarios.

The effective spin Hall angle, ξ_{DL}, is determined by the equation $\chi = (\pi/2)\,[\hbar\xi_{\text{DL}}/(2e\mu_0 M_s t_{\text{FM}})]$,[50] where $\hbar$, e, μ_0, M_s, and t_{FM} denote the reduced Planck constant, the electron charge, the vacuum permeability, the saturation magnetization, and the FM layer thickness, respectively. As illustrated in Fig. 6(f), the SF system with $t_{\text{Ir}} = 1$ nm yields a calculated ξ_{DL} value of 0.115, which aligns with the intrinsic spin Hall angle of Pt,[5] validating the reliability of the measurement methodology. For the SAF samples with $t_{\text{Ir}} = 0.5$ nm, a significantly enhanced ξ_{DL} value of 0.523 is observed. This substantial enhancement in the effective spin Hall angle can be attributed to the antiferromagnetic coupling.[35]

4. Conclusion

In this work, the influence of IEC on SOT effects in SAF and SF was systematically investigated, with particular focus on magnetization switching, critical switching current density, and SOT efficiency. The modulation of IEC in both SAF and SF structures was achieved through precise tuning of the Ir spacer thickness. Experimental results demonstrated that the critical switching current density increases linearly with IEC strength, irrespective of coupling type. Analysis based on the LLG equation revealed that this linear relationship originates from the contribution of the interlayer exchange coupling field to the total energy barrier that must be overcome during SOT-induced switching.

Significantly higher SOT efficiency was observed with antiferromagnetic coupling compared to ferromagnetic coupling, with SOT efficiency being proportional to the antiferromagnetic exchange coupling field. In practical applications, a fundamental trade-off exists between reducing the switching current density and enhancing data stability through increased IEC. Strong IEC elevates the energy barrier, substantially reducing the probability of spontaneous switching under thermal excitation, thereby improving data stability, albeit at the cost of a slight increase in J_c. Therefore, understanding the IEC–J_c relationship enables optimization of critical industry metrics through strategic trade-offs among tunneling magnetoresistance, write power consumption, magnetic interference immunity, data retention, and write error rate.

Acknowledgments

Project supported by the "Pioneer" and "Leading Goose" R&D Program of Zhejiang Province (Grant No. 2022C01053), the Key Research and Development Program of Zhejiang Province (Grant No. 2021C01039), the National Natural Science Foundation of China (Grant No. 62293493), and the Natural Science Foundation of Zhejiang Province, China (Grant No. LQ21A050001).

References

[1] Liu L, Yu J, González-Hernández R, Li C, Deng J Y. Lin W N, Zhou C H, Zhou T J, Zhou J, Wang H, Guo R, Yoong H Y, Chow G M, Han X F, Dupé B, Železný J, Sinova J and Chen J S 2020 *Phys. Rev. B* **101** 220402

[2] Sinova, J, Valenzuela, S O, Wunderlich J, Back C H and Jungwirth T 2015 *Rev. Mod. Phys.* **87** 1213

[3] Song Q, Mi J, Zhao D, Su T, Yuan W, Xing W Y, Chen Y Y, Wang T Y, Wu T, Chen X H, Xie X C, Zhang C, Shi J and Han W 2016 *Nat. Commun.* **7** 13485

[4] Shao Q M, Li P, Liu L Q, Yang H, Fukami S, Razavi A, Wu H, Wang K, Freimuth F, Mokrousov Y, Stiles M D, Emori S, Hoffmann A, Akerman J, Roy K, Wang J P, Yang S H, Garello K and Zhang W 2021 *IEEE Trans. Magn.* **57** 800439

[5] Zhu L J, Ralph D C and Buhrman R A 2021 *Appl. Phys. Rev.* **8** 031308

[6] Liu L Q, Pai C F, Li Y, Tseng H W, Ralph D C and Buhrman R A 2012 *Science* **336** 555

[7] Liu L Q, Lee O J, Gudmundsen T J, Ralph D C and Buhrman R A 2012 *Phys. Rev. Lett.* **109** 096602

[8] Fan H D, Shao Z J, Wang J L, Jin M H, Wu B R, Feng Z S, Wei M Z, Yu C Q, Wen J H, Li H, Chen T W, Liu B, Li W J and Zhou T J 2023 *Phys. Rev. B* **108** 224409

[9] Han X F, Wang X, Wan C H, Yu G Q and Lv X R 2021 *Appl. Phys. Lett.* **118** 120502

[10] Yu G Q, Upadhyaya P, Fan Y B, Alzate J G, Jiang W J, Wong K L, Takei S, Bender S A, Chang L T, Jiang Y, Lang M R, Tang J S, Wang Y, Tserkovnyak Y, Amiri P K and Wang K L 2014 *Nat. Nanotechnol.* **9** 548

[11] Liu L, Zhou C H, Shu X Y, Li C J, Zhao T Y, Lin W N, Deng J Y, Xie Q D, Chen S H, Zhou J, Guo R, Wang H, Yu J H, Shi S, Yang P, Pennycook S, Manchon A and Chen J S 2021 *Nat. Nanotechnol.* **16** 277

[12] Shu X Y, Liu L, Zhou J, Lin W N, Xie Q D, Zhao T Y, Zhou C H, Chen S H, Wang H, Chai J W, Ding Y S, Chen W and Chen J S 2022 *Phys. Rev. Appl.* **17** 024031

[13] Shi G Y, Wan C H, Chang Y S, Li F, Zhou X J, Zhang P X, Cai J W, Han X F, Pan F and Song C 2017 *Phys. Rev. B* **95** 104435

[14] Haazen P P J, Mure E, Franken J H, Lavrijsen R, Swagten H J M and Koopmans B 2013 *Nat. Mater.* **12** 299

[15] Zhou Z Y, Cheng X K, Hu M L, Chu R Y, Bai H, Han L, Liu J W, Pan F and Song C 2025 *Nature* **638** 645

[16] Higo T, Kondou K, Nomoto T, Shiga M, Sakamoto S, Chen X Z, Nishio-Hamane D, Arita R, Otani Y, Miwa S and Nakatsuji S 2022 *Nature* **607** 474

[17] Qin P X, Yan H, Wang X N, Chen H Y, Meng Z, Dong J T, Zhu M, Cai J L, Feng Z X, Zhou X R, Liu L, Zhang T L, Zeng Z M, Zhang J, Jiang C B and Liu Z Q 2023 *Nature* **613** 485

[18] Hu S, Shao D F, Yang H L, Pan C, Fu Z X, Tang M, Yang Y M, Fan W J, Zhou S M, Tsymbal E Y and Qiu X P 2022 *Nat. Commun.* **13** 4447

[19] Krempaský J, Šmejkal L, D'souza S W, *et al.* 2024 *Nature* **626** 517

[20] Chen X Z, Higo T, Tanaka K, Nomoto T, Tsai H, Idzuchi H, Shiga M, Sakamoto S, Ando R, Kosaki H, Matsuo T, Nishio-Hamane D, Arita R, Miwa S and Nakatsuji S 2023 *Nature* **613** 490

[21] Chen H Y, Liu L, Zhou X R, Meng Z, Wang X N, Duan Z Y, Zhao G J, Yan H, Qin P X and Liu Z Q 2024 *Adv. Mater.* **36** 2310379

[22] Duine R A, Lee K J, Parkin S S P and Stiles M D 2018 *Nat. Phys.* **14** 217

[23] Zhu L J 2023 *Adv. Mater.* **35** 2300853

[24] Chen R Y, Gao Y, Zhang X C, Zhang R Q, Yin S Q, Chen X Z, Zhou X F, Zhou Y J, Xia J, Zhou Y, Wang S G, Pan F, Zhang Y and Song C 2020 *Nano. Lett.* **20** 3299

[25] Wang Z L, Li P Z, Fattouhi M, Yao Y X, Hees Y L W V, Schippers C F, Zhang X Y, Lavrijsen R, Garcia-Sanchez F, Martinez E, Fert A, Zhao W S and Koopmans B 2023 *Cell Rep. Phys. Sci.* **4** 101334

[26] Wang Q H, Ni M Y, Li S J, Zheng F W, Lu H Y and Zhang P 2024 *Chin. Phys. Lett.* **41** 057401

[27] Bi C, Almasi H, Price K, Newhouse-Illige T, Xu M, Allen S R, Fan X and Wang W G 2017 *Phys. Rev. B* **95** 104434

[28] Xie X J, Wang X J, Wang W, Zhao X N, Bai L H, Chen Y X, Tian Y F and Yan S S 2023 *Adv. Mater.* **35** 2208275

[29] Parkin S S P 1991 *Phys. Rev. Lett.* **67** 3598

[30] Yoshida C, Takenaga T, Iba Y, Yamazaki Y, Noshiro H, Tsunoda K, Hatada A, Nakabayashi M, Takahashi A, Aoki M and Sugii T 2013 *IEEE Trans. Magn.* **49** 4363

[31] Fan H D, Wei M Z, Feng Z S, Wu B R, Jin M H, Shao Z J, Yu C Q, Liu B, Li W J and Zhou T J 2025 *Phys. Rev. Mater.* **9** 044402

[32] Zhang T F, Wang Q W, Chen M, Dong J, Zhao Q, Li Z M, Liu Q F, Wang J B and Wei J W 2025 *Chin. Phys. B* **34** 057201

[33] Zhang R Q, Shi G Y, Su J, Shang Y X, Cai J W, Liao L Y, Pan F and Song C 2020 *Appl. Phys. Lett.* **117** 212403

[34] Fan H D, Jin M H, Luo Y M, Yang H X, Wu B R, Feng Z S, Zhuang Y S, Shao Z J, Yu C Q, Li H, Wen J H, Wang N N, Liu B, Li W J and Zhou T J 2023 *Adv. Funct. Mater.* **33** 2211953

[35] Zhang P X, Liao L Y, Shi G Y, Zhang R Q, Wu H Q, Wang Y Y, Pan F and Song C 2018 *Phys. Rev. B* **97** 214403

[36] Yakushiji K, Sugihara A, Fukushima A, Kubota H and Yuasa S 2017 *Appl. Phys. Lett.* **110** 092406

[37] Li Z S, Fei Y N, Chen L, Zhan X, Yang L P, Yan C J, Wang W Q, Zhou K Y, Li H T, Ma F S, Zhou T J, Du Y W and Liu R H 2022 *Phys. Rev. B* **105** 184419

[38] Li Y, Jin X J, Pan P F, Tan F N, Lew W S and Ma F S 2018 *Chin. Phys. B* **27** 127502

[39] Feng Z S, Yu C Q, Huang H X, Fan H D, Wei M Z, Wu B R, Jin M H, Zhuang Y S, Shao Z J, Li H, Wen J H, Zhang J, Zhang X F, Wang N N, Mu S and Zhou T J 2023 *Chin. Phys. B* **32** 048504

[40] Saito Y, Tezuka N, Ikeda S and Endoh T 2021 *Phys. Rev. B* **104** 064439

[41] Parkin S S P and Mauri D 1991 *Phys. Rev. B* **44** 7131

[42] Shen B W, Yang M Y, Li Y R, Yu P Y, Gao J F, Cui B S, Yu G Q and Luo J 2024 *Appl. Phys. Lett.* **124** 012401

[43] Saito Y, Ikeda S and Endoh T 2022 *Phys. Rev. B* **105** 054421

[44] Fan H D, Jin M H, Wu B R, Wei M Z, Wang J L, Shao Z J, Yu C Q, Wen J H, Li H, Li W J and Zhou T J 2023 *Appl. Phys. Lett.* **122** 262404

[45] Ma Q L, Li Y F, Choi Y S, Chen W C, Han S J and Chien C L 2020 *Appl. Phys. Lett.* **117** 172403

[46] Liu L, Zhao X T, Liu W, Song Y H, Zhao X G and Zhang Z D 2021 *J. Phys. D: Appl. Phys.* **54** 505003

[47] Fache T, Rojas-Sanchez J C, Badie L, Mangin S and Petit-Watelot S 2020 *Phys. Rev. B* **102** 064425

[48] Ishikuro Y, Kawaguchi M, Taniguchi T and Hayashi M 2020 *Phys. Rev. B* **101** 014404

[49] Chuang T C, Pai C F and Huang S Y 2019 *Phys. Rev. Appl.* **11** 061005

[50] Pai C F, Mann M, Tan A J and Beach G S D 2016 *Phys. Rev. B* **93** 144409